Engenharia Agrícola

ISSN: 1809-4430 (on-line)

www.engenhariaagricola.org.br

Scientific Paper
Doi: http://dx.doi.org/10.1590/1809-4430-Eng.Agric.v42n2e20210226/2022

SIMULATION OPTIMIZATION AND EXPERIMENTAL STUDY OF THE AIR DISTRIBUTION CHAMBER STRUCTURE OF STRAW-BASED NUTRIENT SEEDING-GROWING BOWL TRAY MICROWAVE–HOT-AIR COUPLING DRYERS

Haiyuan Li[1,2], Yuhui Hu[1], Lianxing Qi[1], Haiming Yu[1*]

[1*]Corresponding author. College of Electrical and Information, Northeast Agricultural University, Harbin, China.
E-mail: hmyu09@yeah.net | ORCID ID: https://orcid.org/0000-0001-6033-4596

KEYWORDS

air distribution chamber structure, CFD model, simulation optimization

ABSTRACT

To improve the flow field structure of the air distribution chamber of the microwave–hot-air coupling dryer for a straw-based nutrient seeding-growing bowl tray and enhance the uniformity of the outlet gas velocity distribution, computational fluid dynamics software was used to simulate the flow field of the air distribution chamber based on the gas motion differential equation and the (RNG) k–ε turbulence model. Using the front panel height, upper apex angle, and side wall inclination angle as factors and the speed nonuniformity coefficient as the index, the results showed that when the air distribution chamber front panel height was 33 mm, the upper apex angle was 108°, the side wall inclination angle was 78°, the height of the two spoilers was 40 mm, the outlet airflow speed varied from 5.36 to 5.71 m/s, and the speed unevenness coefficient was reduced from 13.95% in the original model to 6.05%. The maximum deviation between the numerical simulation results and test data was less than 4%, which met the uniformity requirement of the outlet airflow speed of the dryer. The results provide theoretical support for the design and industrial production of microwave–hot-air coupling dryers.

INTRODUCTION

The total amount of crop straw produced in China is approximately 1 billion tons per year, which ranks first worldwide (Guo & Huang, 2016). Currently, straw is mainly utilized to produce energy, feed, and raw material, as well as in fertiliser application in the field (Wang et al., 2017). However, approximately 200 million tons of straw produced every year are not effectively utilised in China (Hu et al., 2018a) as surplus straw is mainly incinerated in the field. Straw burning not only wastes resources and causes environmental pollution but also destroys the ability of the soil to resist drought and moisture. Therefore, the utilisation of excess straw has become an urgent problem.

Straw-based nutrient seeding-growing bowl trays (also referred to as nutritious bowl trays) use crop straw as the main raw material. To prepare a nutritious bowl tray for rice production, nutrient additives and anti-sterilisation drugs necessary for rice growth are simultaneously added to the crop straw and subsequently subjected to air pressure forming, drying stereotypes, and other processing techniques (Liu et al., 2012; Zhang et al., 2013). Although the production of nutritious bowl tray consumes a large amount of crop straw, it also increases the utility of straw resources. Nutritious bowl trays have the advantages of storing and conserving water, improving soil fertility, prolonging the rice growth period, and increasing rice output, thus increasing the income of farmers (Chen & Yang, 2017; Chen et al., 2005; Han et al., 2011; Li et al., 2014; Cai et al., 2018). Additionally, during the production of nutritious bowl tray, the moisture content is high and the strength is low after subjection to vacuum adsorption moulding, which do not meet the requirements of sowing, seedling, transplanting, and transportation. Therefore, after vacuum adsorption moulding, the tray must be dried to meet the production requirements (Yu et al., 2014). Current drying methods of nutritious bowl trays mainly include natural and hot-air drying. Naturally dried trays, which are considerably affected by the natural environment, have a low drying efficiency, low strength after drying, and severe warpage, which significantly

[1] College of Electrical and Information, Northeast Agricultural University, Harbin, China.
[2] College of Mechanical and Automotive Engineering, Zhaoqing University, Zhaoqing, China.

Area Editor: Gizele Ingrid Gadotti
Received in: 12-14-2021
Accepted in: 3-1-2022

affects their quality and the subsequent rice production. Although hot-air drying can satisfy the drying quality requirements of nutritious bowl trays, it has low efficiency and high energy consumption, which increases production costs and hinders the further promotion and application of nutritious bowl trays. Therefore, there is an urgent need to apply a new method for the drying of nutritious bowl trays. Microwave–hot-air coupling drying technology is a process in which microwave radiation and hot air act on the dry material at the same time. Combining the advantages of hot-air and microwave drying, this technology has a faster drying rate and higher drying quality than either microwave or hot-air drying (Yu et al., 2015a; Yu et al., 2015b). Drying technology with broad development prospects has been widely used in agricultural production (Horuz et al., 2017; Ma et al., 1997; Wang et al., 2018), agricultural product processing, and the food industry. To date, no scholar has applied microwave–hot-air coupling drying technology for nutritious bowl tray drying. Hence, research on a suitable microwave–hot-air coupling dryer (thereafter referred to as dryer) is the key to the realisation of the microwave–hot-air coupling drying of nutritious bowl trays.

In the dryer, the air distribution chamber plays an important role in optimising the flow field distribution and evenly distributing the gas flow rate. Thus, an unreasonable structural design will lead to inconsistent gas flow speeds at the air outlet of the distribution chamber, which affects the uniform distribution of the temperature field in the drying chamber and subsequently the drying quality, drying time, and energy consumption of the tray (Yu, 2015). In recent years, computational fluid dynamics (CFD) has been widely used for flow-field analysis and structural optimisation in some devices. Pan et al. (2009) calculated the velocity distribution between multiple parallel channels with triangular manifolds using a three-dimensional CFD model. They also analysed the influence of structural parameters on the velocity distribution between the channels. The results showed that the longer the channel length, the deeper the depth, and the smaller the width, the more uniform the velocity distribution. A symmetrical structure facilitates a uniform distribution of flow velocity between channels than an asymmetric manifold structure Hassan et al. (2014) studied the uniformity of the fluid distribution under different cavity structures. The CFD simulation and test of circular cross-section and conical section manifolds were analysed by evaluating the water conservancy parameters of each outlet. The experimental results showed that the flow velocity distribution of the circular cross-section manifold exit was severely uneven, whereas that of the conical section manifold was almost uniform, and the simulation results exhibited the same trend as the experimental data. Meanwhile, Tang et al. (2019) used CFD numerical simulation method to simulate and analyse the outflow field of a beekeeping vehicle with and without a tailgate. The results showed that with and without the tailgate, the velocity and pressure distributions of the front and both sides of the beekeeping vehicle were roughly the same, and there were significant differences between the pedestrian corridor area and the rear part of the vehicle. Zhou et al. (2021) studied the gas flow field distribution law of a stereo-swirling sieve tray using different structural parameters and installation methods. The optimisation results showed that the tray structure was composed of eight blades with a blade twist angle of 90° and a tray height of 40 mm. When the sieve diameter was 5 mm, the tray had the best performance, and the distribution of the gas flow field in the sieve tray was more uniform, providing a reference for the study of internal members with similar structures. Zheng et al. (2015) used CFD to simulate the seepage of a cracking liquid during the fracturing process of unconventional reservoirs. The influence of outlet structure on the flow state and erosion rate was also investigated, and the experimental results showed that the optimised hydraulic pressure of the fracturing structure could be reduced by approximately 40%, whereas the average erosion rate of the fracturing tool could be reduced by approximately 50%. Structural optimisation can improve the erosion life of fracturing tools. However, the use of CFD to study the flow field and structural optimisation of the air distribution chamber in a drying unit has rarely been reported in the literature. Although Xu et al. (2005) optimised the gas distribution chamber of a gas wall-hanging boiler, there is lack of data support and experimental comparison. Tian and Gao proposed an improved design for the problem of uneven nozzle exit velocity in an oven air distribution chamber; however, the optimisation model is too single and lacks test verification. Hu et al. (2018b) analysed the influence of increasing the deflector, changing its installation position and thickness, and other factors on the uniformity of the velocity of the duct in the drying chamber. However, there was little analysis of the flow field in the drying chamber and a lack of analysis of the interaction between the factors affecting the uniformity of the flow field in the drying chamber.

In this study, an airflow field model was established for the air distribution chamber of a nutritious bowl-tray microwave–hot-air coupling dryer. CFD software was used for numerical simulations. The unevenness coefficient of the outlet velocity was used as an evaluation index to investigate the effect of the air distribution cavity structure on the uniformity of the flow velocity distribution. The model was further improved by adding a spoiler, and the accuracy and rationality of the simulation results were experimentally verified to provide theoretical support for the design and industrial production of microwave–hot-air coupling dryers and technical support for the industrial production of nutritious bowl trays.

MATERIAL AND METHODS

Instruments and equipment

The hot-air-assisted microwave intermittent drying equipment for the nutritious bowl tray used in this experiment was modified from the YHMW900-100 microwave–hot-air coupling multifunctional dryer. Fig. 1 shows the structure and physical objects. The equipment has the functions of microwave, hot-air, and microwave–hot-air drying. It is mainly composed of a microwave drying system, a hot-air drying system, and a control system. The overall dimensions are 1570 mm (height) × 1000 mm (width) × 505 mm (thickness). The microwave drying system mainly comprises a waveguide, microwave generator (magnetron), and microwave resonant cavity (drying chamber). The structure of the microwave resonant cavity has dimensions of 330 mm (length) × 350 mm (width) × 215 mm (height). The microwave power is 1.3 kW and the output power is 0.9 kW. Meanwhile, the hot-air drying system is mainly composed of an airflow distribution room, heater, airflow initial distribution stabiliser, and centrifugal fan with a power of 550 W. The heater comprises three far-infrared carbon fibre heating tubes (electric heating rods) and heating tubes (white steel tubes) with a power of 800 W. The microwave and hot-air drying systems are connected by an airflow distribution chamber and an airflow initial distribution stabiliser so that the hot air is evenly disseminated into the microwave resonance cavity. The control system is mainly composed of an airflow velocity sensor, temperature sensor, microwave regulator, time regulator, frequency converter, and control display instrument.

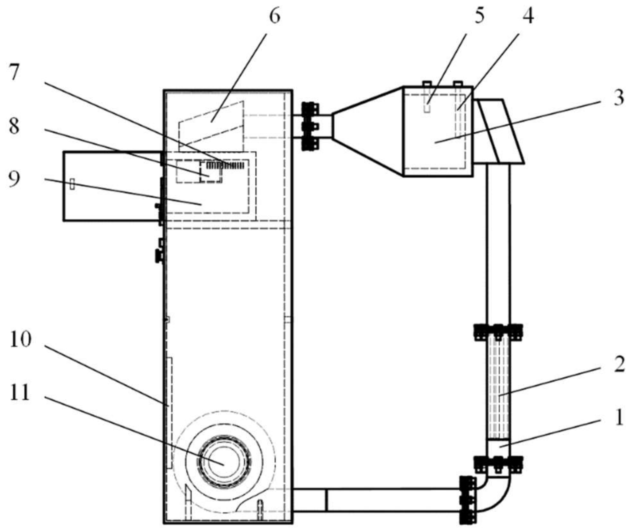

(a) Structure (b) Physical map

1. Heating tube; 2. Electric heating rod; 3. Air flow initial distribution stabilizer; 4. Temperature sensor; 5. Air flow velocity sensor; 6. Air flow distribution chamber; 7. Drain hole; 8. Microwave generator; 9. Microwave resonant cavity (drying chamber); 10. Control system; 11. Fan

FIGURE 1. Diagram of the structure and physical map of a microwave coupled with hot-air dryer

Original physical model and meshing of the airflow distribution chamber

The air distribution chamber is mainly composed of an air inlet end, air distribution chamber, and air outlet end, as shown in Fig. 2(a) and (b). The inlet end was located behind the air distribution chamber, with a diameter D of 89 mm. Meanwhile, the original physical model of the air distribution chamber did not consider flow-field structure optimisation. The bottom surface size (length × width) was 250×250 mm and the front panel height of the cavity was X_1 = 20 mm. The height of the back panel of the cavity was H = 209 mm, the apex angle of the cavity was X_2 = 100°, and the inclination angle of the side wall was X_3 = 90°. The air outlets were distributed in a matrix arrangement on the surface of the air distribution chamber, and there were 12 rows, with each column having 12 air outlets. The air outlet spacing was 19.85 mm and the diameter was 8 mm. The air outlet of the leftmost end of the original model front view of the distribution room was set as the first list of air outlets, whereas the rightmost end was set as the 12th list.

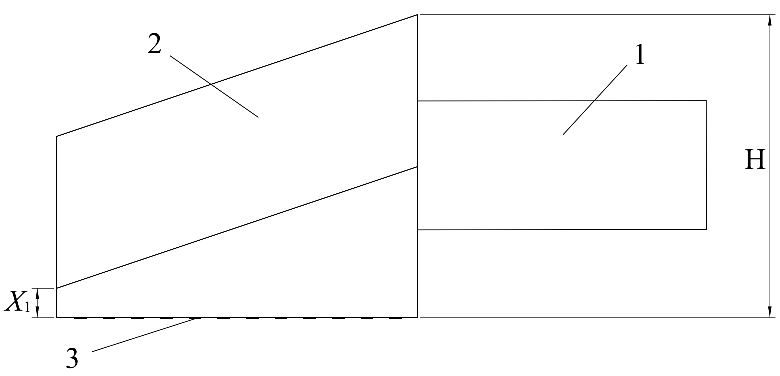

(a) Front view of the original model

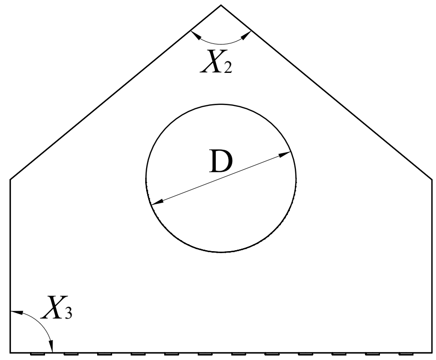

(b) Left view of the original model

1. Air inlet end; 2. Air distribution chamber; 3. Outlet end

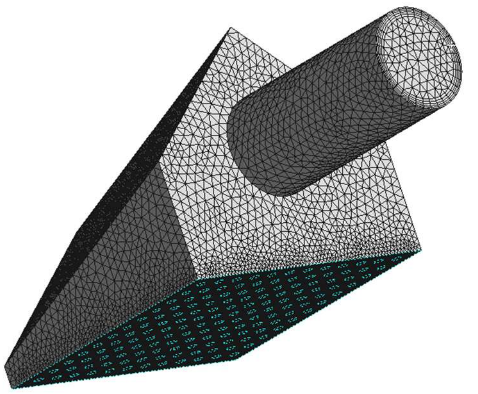

(c) Schematic diagram of the grid

FIGURE 2. Schematic diagram of the original model structure and grid.

The establishment of geometric models and meshing plays a key role in the analysis process. The three-dimensional model of the air distribution chamber established according to the design requirements was imported into ANSYS FLUENT, and the inner flow channel was extracted as the indoor flow field model of the air distribution chamber. The MESH module was used to mesh the physical model, and the mesh type was a tetrahedral element. An unstructured meshing method was used to locally encrypt the faces of the entrance and exit to improve the calculation accuracy and smoothen the mesh. Subsequently, the equivolume skewness was less than 0.9. Fig. 2(c) shows the meshing results. The total number of physical model meshes was approximately 1.26 million.

Gas control equations

Considering the balance between simulation efficiency and precision, we made the following assumptions for the physical model: (1) The air distribution chamber cavity is well sealed, and there is no air leakage. (2) The indoor hot air flow is a steady-state viscous flow. (3) Owing to the low flow velocity in the cavity, the airflow is regarded as an incompressible gas. (4) The airflow in the cavity is steadily turbulent.

Based on the above assumptions, it was determined that the gas flow state satisfied the continuity and momentum conservation equations (Li & Wang, 2007; Qu et al., 2011; Kalman et al., 2000) given by eqs (1) and (2), respectively:

$$\frac{\partial u_i}{\partial x_i} = 0 \tag{1}$$

$$\rho \frac{\partial (u_i u_j)}{\partial x_j} = \frac{\partial}{\partial x_j}\left[\mu\left(\frac{\partial u_i}{\partial x_j} + \frac{\partial u_j}{\partial x_i}\right) - \frac{2}{3}\mu \delta_{ij}\frac{\partial u_k}{\partial x_k}\right] - \frac{\partial p}{\partial x_i} \tag{2}$$

Where:

ρ is the fluid density, kg/m^3;

u_i and u_j are the average velocity components (i, j = 1, 2, 3), m/s;

p is the time constant pressure of the fluid, N/m^2;

μ is the hydrodynamic viscosity, N·s/m^2;

x_i and x_j are coordinate components, and

δ_{ij} is a function such that when $i = j$, δ_{ij} = 1, and when $i \neq j$, δ_{ij} = 0.

Considering the airflow in the vent, expansion, and curved wall of the distribution chamber, we adopted the renormalisation group (RNG) $k \sim \varepsilon$ turbulence model, which has a better performance than the standard $k \sim \varepsilon$ turbulence model (Yakhot & Orszag, 1986), to simulate the airflow distribution cavity. The turbulence energy k and dissipation rate ε equations are given by eqs (3) and (4), respectively:

$$\rho \frac{dk}{dt} = \frac{\partial}{\partial x_i}\left[(\alpha_k \mu_{eff})\frac{\partial k}{\partial x_i}\right] + G_k + G_b - \rho\varepsilon - Y_M \tag{3}$$

$$\rho \frac{d\varepsilon}{dt} = \frac{\partial}{\partial x_i}\left[(\alpha_\varepsilon \mu_{eff})\frac{\partial \varepsilon}{\partial x_i}\right] + C_{1\varepsilon}\frac{\varepsilon}{k}(G_k + C_{3\varepsilon}G_b) - C_{2\varepsilon}\rho\frac{\varepsilon^2}{k} - R \tag{4}$$

Where:

G_k is the turbulent energy generated due to the average velocity gradient;

G_b is the turbulent energy generated due to the influence of buoyancy;

Y_M is the effect of compressible turbulent pulsation expansion on the total dissipation rate;

α_k and α_ε are the reciprocals of the effective turbulent Prandtl number of the kinetic energy k and dissipation rate ε, and the k and ε turbulent Prandtl numbers are σ_k= 1.0 and σ_ε= 1.3, respectively;

$C_{1\varepsilon}$, $C_{2\varepsilon}$, and $C_{3\varepsilon}$ default constants, which are 1.44, 1.92, and 0.09, respectively.

The formula for calculating the turbulent viscosity coefficient is given by:

$$d\left(\frac{\rho^2 k}{\sqrt{\varepsilon\mu}}\right) = 1.72\frac{\tilde{v}}{\sqrt{\tilde{v}^{-3} - 1 - C_v}}d\tilde{v} \tag{5}$$

Where:

$\tilde{v} = \mu_{eff}/\mu$, μ_{eff} is the equivalent viscosity coefficient, and $\mu_{eff} = \mu + \mu_t$. In FLUENT software, the default setting (RNG) $k \sim \varepsilon$ is for flow problems with high Reynolds number. For high Reynolds numbers, $\mu_t = \rho C_\mu k^2/\varepsilon$, C_μ = 0.0845; C_v is the default constant, $C_v \approx 100$.

Boundary conditions and solution calculation method

The fluid power at the inlet end was set by the fan, and air was used as the fluid. The inlet and outlet fluid temperatures of the given air distribution chamber were both 333 K, the air density was 1.06 kg/m^3, and the viscosity coefficient was 2.01×10^{-5} Pa·s. A speed inlet was adopted at the inlet end. The turbulence model was combined with the Reynolds number and turbulence intensity calculation equations to obtain a turbulence intensity of 3.4% (Yu et al., 2008). The inlet speed was set to 5 m/s in combination with the actual working conditions, and the outlet of the distribution chamber was set as the pressure outlet. The atmospheric pressure was the boundary value, and the turbulence intensity at the outlet end was set to 5%. The residual accuracy was set to 10^{-5}, and the remaining walls were treated using the standard wall function method (Sun & Li, 2013; Knopp et al. 2006).

Original model calculation analysis and verification

Calculation and analysis of the original model

Figure 3 shows the flow pattern distribution map of hot airflow in the original model and the average speed line diagram corresponding to each column exit. As shown in the figure, the air distribution chamber changed the flow field distribution inside the distribution chamber using a slope. However, owing to the airflow inertia, the slope angle of the original model was too oblique. After the hot airflow entered the air inlet, it entered the distribution chamber. However, there was insufficient space to distribute the airflow, and the speed distribution effect of "front high and rear low" was formed, resulting in a large airflow velocity corresponding to the exit. It was confirmed from Fig. 3(b) that the velocity of the outlet airflow in each column varied between 5.4 and 6.87 m/s. The outlet airflow velocity significantly increased from

6.01 m/s in the first column to 6.87 m/s in the second column. Subsequently, it decreased to 5.41 m/s in the eighth column and then stabilized. The speed unevenness coefficient was 13.95%, which did not satisfy the uniform drying requirement of the drying machine. Hence, the original model structure needs to be optimised.

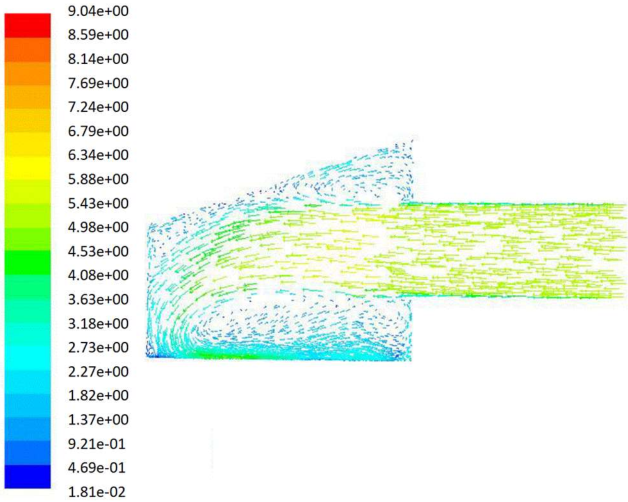

(a) Velocity distribution vector diagram

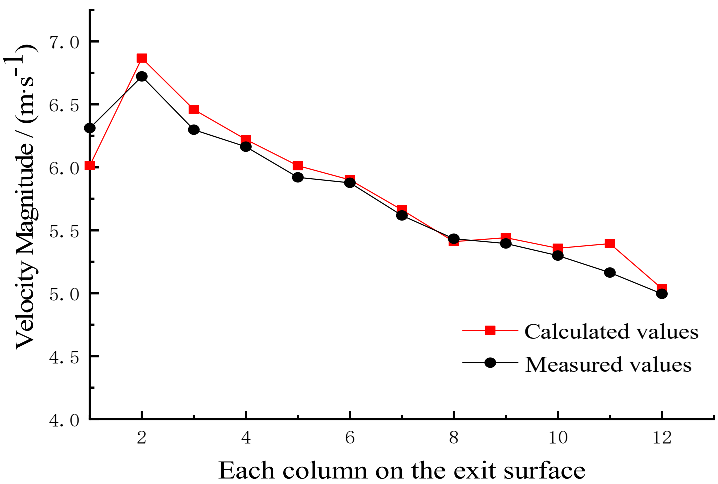

(b) Average velocity distribution in each column on the exit surface

FIGURE 3. Original model flow field feature distribution map.

Original model calculation test verification

The original model of the airflow distribution chamber of the dryer was verified to further demonstrate the accuracy of the numerical simulation. By analysing the correlation between the calculated values of the outlet flow rates of the original model of the air distribution chamber and the measured values, it was determined whether the mathematical model established in this study met the test requirements. The linear correlation fitting method can be used to compare the differences between discrete data more accurately (Ding et al., 2016 Zhou et al., 2012). Fig. 4 shows a linear analysis of the measured and calculated values of the flow velocity of each air outlet in the air distribution chamber. The correlation curve was y = 0.98409x + 0.13793, and the coefficient R^2 = 0.94081. Moreover, the flow of the mathematical model was observed, and the field distribution characteristics were consistent with the measured values, which, in turn, were consistent with the calculated values. Meanwhile, the deviation between the two values was within the allowable range of the calculation. This indicates that the hydrodynamic calculation method can be used to determine the evaluation index of the simulation test to determine the optimal structure of the airflow distribution chamber.

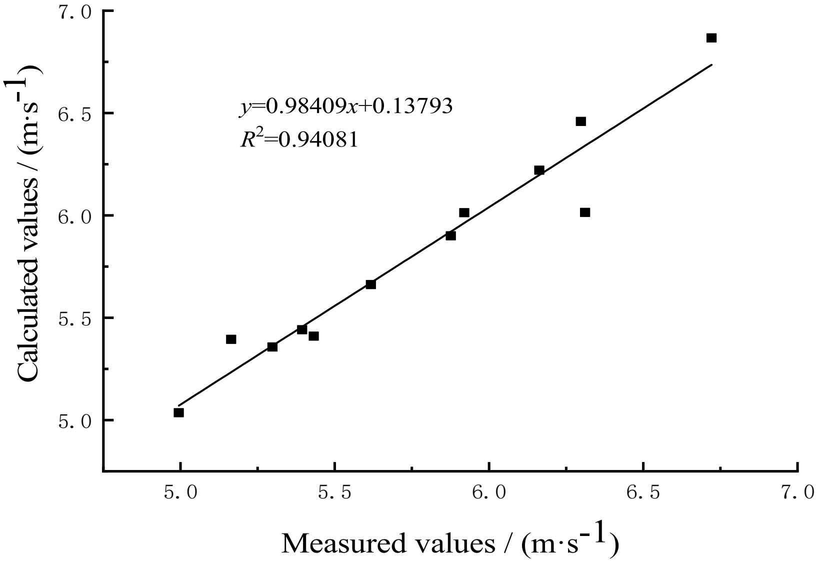

FIGURE 4. Correlation analysis between the original model physical map and the measured and calculated values.

RESULTS AND DISCUSSION

Simulation test factors and scope determination

Considering that the original model slope was too inclined, the hot-air flow entered the air inlet end of the air distribution chamber and was fan-shaped directly to the front ends of the chamber and outlet owing to inertia. Because there was insufficient reserved space in the chamber, the front and rear flow rates of the exits of each column were uneven. According to the relevant literature (Tian & Gao, 2009), the height of the airflow distribution chamber front panel X_1, top angle of the cavity X_2, and inclination angle of the side wall X_3 were selected as the influencing factors. Based on previous research, the range of the influencing factors was determined as follows: X_1= 28–36 mm, X_2= 105–115°, and X_3= 85–75°.

Determination of evaluation indicators

To quantitatively compare the airflow uniformity of each outlet surface of the air distribution chamber, the velocity nonuniformity coefficient *M* was used to evaluate the uniformity of the velocity distribution (Han et al., 2005; Lei et al., 2011). The lower the *M* value, the smaller the deviation of the air velocity between the outlets of each column and the more uniform the airflow field distribution. The calculation formula is given by [eq. (6)]:

$$M = \frac{\sqrt{\frac{1}{n-1}\sum_{i=1}^{n}(V_i - \overline{V_a})^2}}{\overline{V_a}} \times 100\% \tag{6}$$

Where:

$\overline{V_a}$ is the overall average velocity distribution (m/s);

V_i is the air velocity at each point (m/s), and

n is the number of exit faces.

Test results and analysis of quadratic regression orthogonal rotation combination simulation

Simulation test plan and results

Based on the principle of quadratic orthogonal rotation combination test design, it was determined that X_1, X_2, and X_3 were the main design independent variables (Yu et al., 2020; Yu et al., 2021). *M* was considered as the evaluation index, and the simulation of the air distribution chamber structure was optimised. Using Design-Expert and CFD software, we obtained the horizontal coding of the test factors, as presented in Table 1. Table 2 presents the test design and results.

TABLE 1. Test factor level coding table.

Coding level	Cavity front plate height X_1 (mm)	Cavity top angle X_2 (°)	Side wall inclination angle X_3 (°)
1.682	39	118	88
1	36	115	85
0	32	110	80
−1	28	105	75
−1.682	25	102	72

TABLE 2. Test design and results.

Test number	Test factor			Test index
	X_1	X_2	X_3	Speed unevenness factor $M/\%$
1	−1	−1	−1	10.1
2	1	−1	−1	9.3
3	−1	1	−1	11.7
4	1	1	−1	11.2
5	−1	−1	1	12.2
6	1	−1	1	11.6
7	−1	1	1	12.9
8	1	1	1	12.3
9	−1.682	0	0	11.3
10	1.682	0	0	10.5
11	0	−1.682	0	10.3
12	0	1.682	0	12.2
13	0	0	−1.682	9.9
14	0	0	1.682	13.1
15	0	0	0	8.5
16	0	0	0	8.6
17	0	0	0	8.7
18	0	0	0	8.4
19	0	0	0	8.5
20	0	0	0	8.8
21	0	0	0	8.5
22	0	0	0	8.7
23	0	0	0	8.6

Analysis of the simulation results

Based on the simulation test results of *M* in Table 2, a multiple regression fitting analysis of the simulation test results was performed using Design-Expert software (Jiang et al., 2015), and the regression equation for *M*, X_1, X_2, and X_3 was obtained, given by [eq. (7)]:

$$M = 8.59-0.28X_1+0.59X_2+0.88X_3+0.037X_1X_2+0.012X_1X_3-0.26X_2X_3+0.82X_1^2+0.95X_2^2+1.04X_3^2 \quad (7)$$

The significance test of the regression equation is presented in Table 3. As shown in the table, the fitting degree of the model was extremely significant (P < 0.01), indicating that the regression model was well fitted and could be used to analyse and predict the test results. The regression terms X_1, X_2, X_3, X_2X_3, X_1^2, X_2^2, and X_3^2 had significant effects, indicating that the three independent variables in the model had considerable effects on the response values. Meanwhile, X_1X_2 and X_1X_3 had no significant effect (P>0.05) and should therefore be eliminated from the regression equation. The lack of fit (P = 0.4525) was not significant, indicating that no other major factor affected the indicator. The insignificant regression terms of the model were eliminated, whereas the significant regression terms of the model were retained. The regression equation of M was simplified by [eq. (8)]:

$$M = 8.59 - 0.28X_1 + 0.59X_2 + 0.88X_3 - 0.26X_2X_3 + 0.82X_1^2 + 0.95X_2^2 + 1.04X_3^2 \quad (8)$$

TABLE 3. Regression equation analysis of variance table.

Variance source	Qualification index			
	Sum of square	Degree of freedom	F	P
Model	58.74	9	397.74	<0.0001**
X_1	1.08	1	65.98	<0.0001**
X_2	4.80	1	292.43	<0.0001**
X_3	10.69	1	651.32	<0.0001**
X_1X_2	0.011	1	0.69	0.4226
X_1X_3	1.250E−003	1	0.076	0.7869
X_2X_3	0.55	1	33.59	<0.0001**
X_1^2	10.81	1	658.48	<0.0001**
X_2^2	14.29	1	870.92	<0.0001**
X_3^2	17.08	1	1040.82	<0.0001**
Residual	0.21	13		
Misfit	0.084	5	0.017	0.4525
Error	0.13	8		
Sum	58.96	22		

Note: **<0.01 (very significant); *<0.05 (significant)

The statistical analysis of the fitting equation error is presented in Table 4. The correlation coefficient R^2 of the model was 0.9964, which proves the correlation and fitting of the equation. The Adj R-Squared and Pred R-Squared values were 0.9939 and 0.9861, respectively, which proves that the selected factors are the main indicators affecting the evaluation. No other significant factors were identified. It can be seen from the above analysis that the regression equation of M has good adaptability, and the regression equation can be used to analyse and predict the test results.

TABLE 4. Statistical analysis of the regression equation error.

Statistical item	Value	Statistical item	Value
Std. Dev.	0.13	R-Squared	0.9964
Mean	10.26	Adj R-Squared	0.9939
C.V./%	1.25	Pred R-Squared	0.9861
PRESS	0.82	Adeq Precision	52.31

Analysis of the influence effect of the test factors

It can be seen from the regression coefficient F test in Table 3 that the influence of X_1, X_2, and X_3 on the index M is $X_3 > X_2 > X_1$ (Li & Hu, 2008; Yu et al., 2013). To reflect the influence of various experimental factors and their interactions on the test evaluation index more clearly and intuitively, the simplified regression model was subjected to the dimensionality reduction, which places each test factor at zero level, and the response surface and contour maps were drawn.

Fig. 5 shows the effect of the interaction between X_1 and X_2 on M. As shown in Fig. 5(a), when the slope angle was X_3 = 80°, M first decreased and then increased with a constant increase in X_1 and X_2. When X_1 varied from 32 to 34 mm and X_2 changed from 107° to 109°, M was low. When X_1 was constant, M first decreased and then increased with an increase in X_2. However, when X_2 was constant, M first decreased and then increased with increasing X_1. The effect of the interaction between X_1 and X_2 on M was not significant. In Fig. 5(b), the rate of change of M along the X_2 direction was higher than that in the X_1 direction; that is, the influence of X_2 on M was greater than that of X_1 on M.

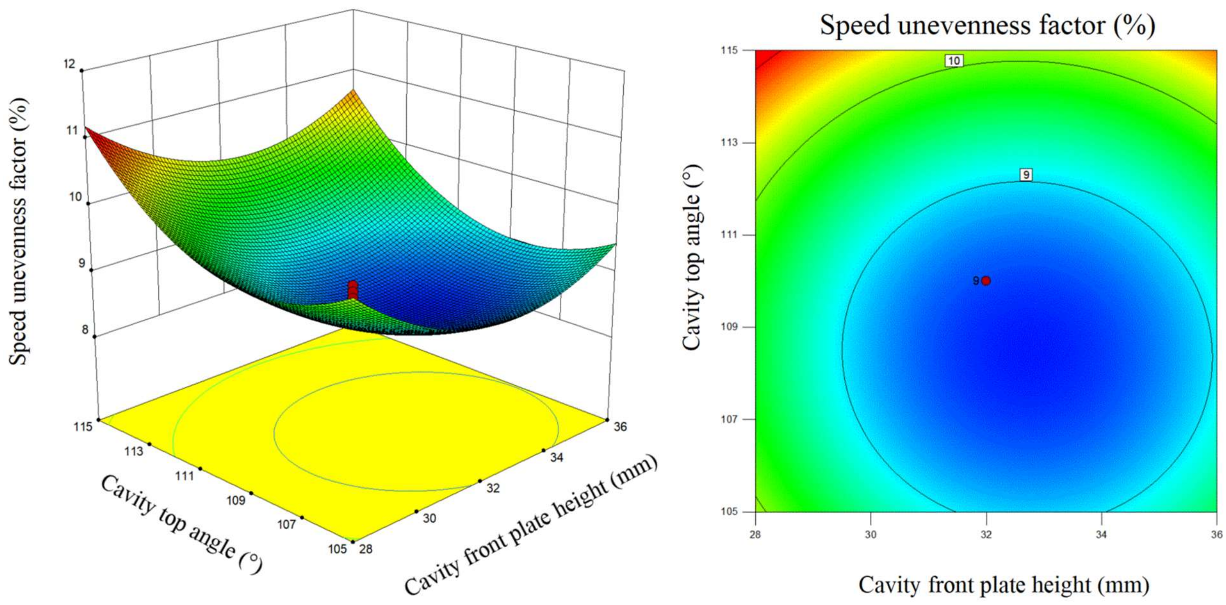

(a) (b)

FIGURE 5. Effect of the height of the front panel and angle of the upper apex on the unevenness coefficient of the outlet velocity of the air distribution chamber.

Figure 6 shows the effect of the interaction between X_1 and X_3 on *M*. It can be seen from Fig. 6(a) that when X_2= 110°, *M* first decreased and then increased as X_1 increased and X_3 decreased. When X_1 was between 32 and 34 mm and X_3 was between 77° and 79°, *M* was low. When X_1 was constant, *M* slightly increased after the first significant decrease with an increase in X_3. However, when X_3 was constant, *M* first decreased and then increased as X_1 increased. The effect of the interaction between X_1 and X_3 on *M* was not significant. In Fig. 6(b), the rate of change of *M* in the X_3 direction was higher than that in the X_1 direction; that is, the influence of X_3 on *M* was greater than that of X_1 on *M*.

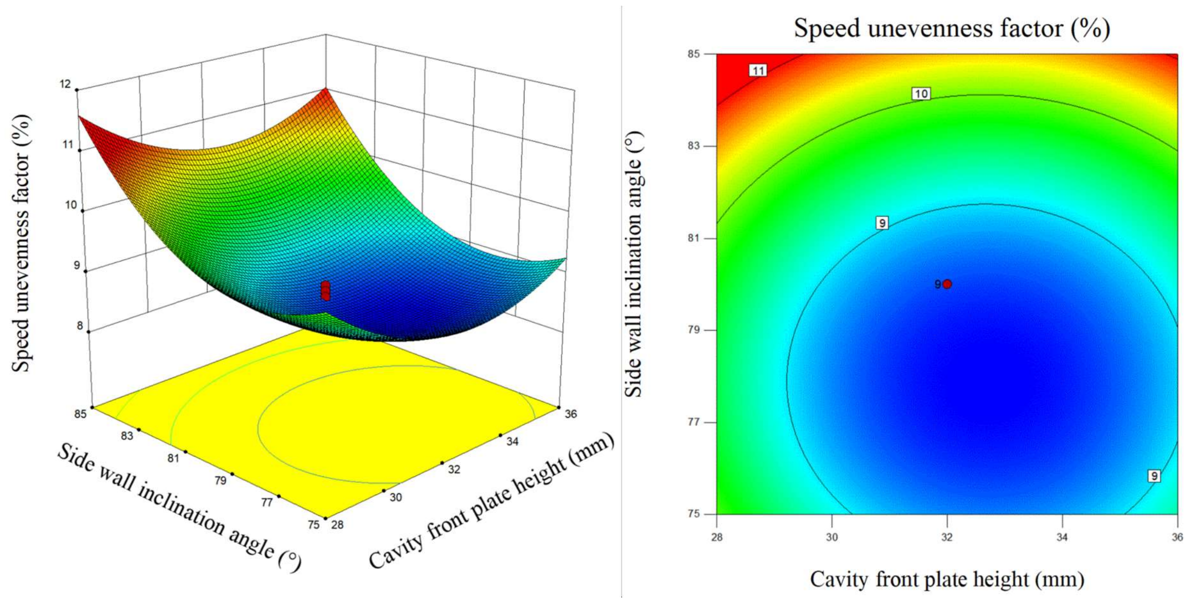

(a) (b)

FIGURE 6. Effect of the height of the front panel and inclination angle of the side wall on the unevenness coefficient of the outlet velocity of the air distribution chamber

Figure 7 shows the effect of the interaction between X_2 and X_3 on *M*. It can be seen from Fig. 7(a) that when X_1= 32 mm, *M* first decreased and then increased as X_2 increased and X_3 decreased. When X_2 varied between 107° and 109° and X_3 varied between 77° and 79°, *M* was low. When X_2 was constant, *M* sharply decreased and then slowly increased as X_3 increased. However, when X_3 was constant, *M* slowly decreased and then sharply increased with an increase in X_2. There was an interaction between the effects of X_2 and X_3

on *M*. The main reason is that as X_2 increased, the original obliquely inclined slope was slowly flattened. As X_3 was gradually reduced, the high airflow velocity zone formed on both sides was instantly exchanged with the central region, reducing *M* at the outlet end. When X_2 and X_3 exceeded a critical value, the hot-air flow obstructed toward the air inlet end became smaller, and the inclination angles on both sides had little or no influence on the hot air flow; thus, the exchange could not develop in the central area, resulting in a corresponding difference in the flow velocity at the outlet end. If the hot-air flow is too large, *M* at the outlet end will increase. In Fig. 7(b), the rate of change of *M* in the X_3 direction was higher than that in the X_2 direction. In other words, the influence of X_3 on *M* was greater than that of X_2 on *M*.

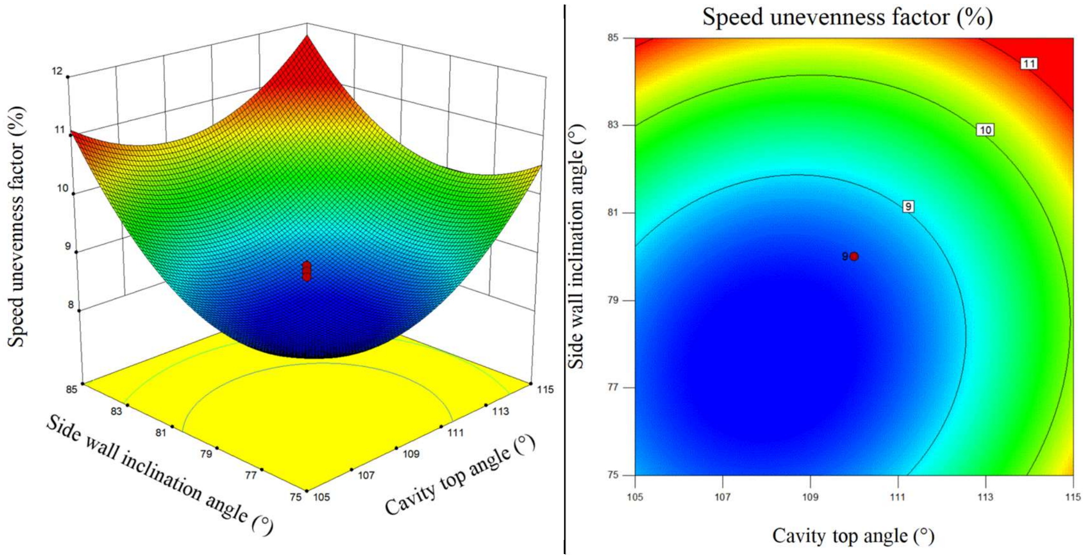

(a) (b)

FIGURE 7. Influence of the top apex angle and slanting angle of the side wall on the unevenness coefficient of the outlet velocity of the air distribution chamber

Optimization and analysis of air distribution chamber structure

To determine the optimal structural parameters of the air distribution chamber, [eq. (9)] was optimised, and the constraints were given as:

$$\begin{cases} 32 \le X_1 \le 34 \\ 107 \le X_2 \le 109 \\ 77 \le X_3 \le 79 \end{cases} \tag{9}$$

The Design-Expert software was used to optimize the solution, and the optimization results of each parameter were obtained as X_1= 33.2 mm, X_2= 108.1°, X_3= 77.8°, and M = 8.68%. The parameters were rounded to facilitate the processing and manufacturing of the air distribution chamber. After rounding, the parameters were X_1= 33 mm, X_2= 108°, and X_3= 78°. An airflow field model was then established and simulated according to the optimised airflow distribution chamber parameters. The average flow velocity line chart and comparison map of *M* values for each column exit surface were obtained, as shown in Fig. 8.

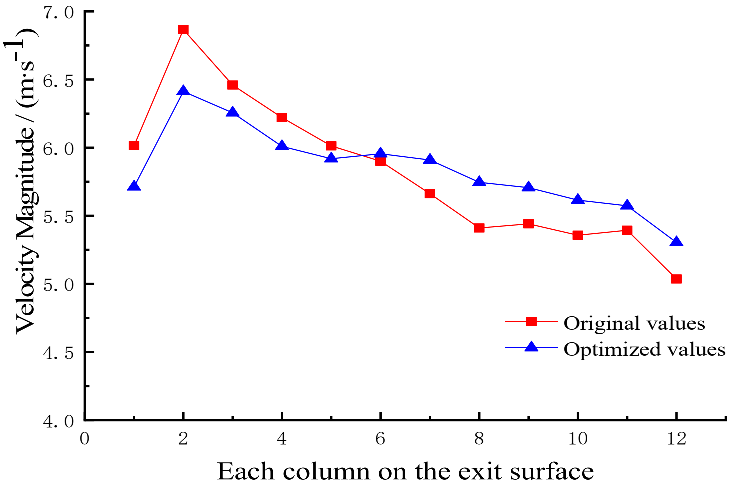

(a) Average flow velocity line chart for each column exit surface of the original and optimized models

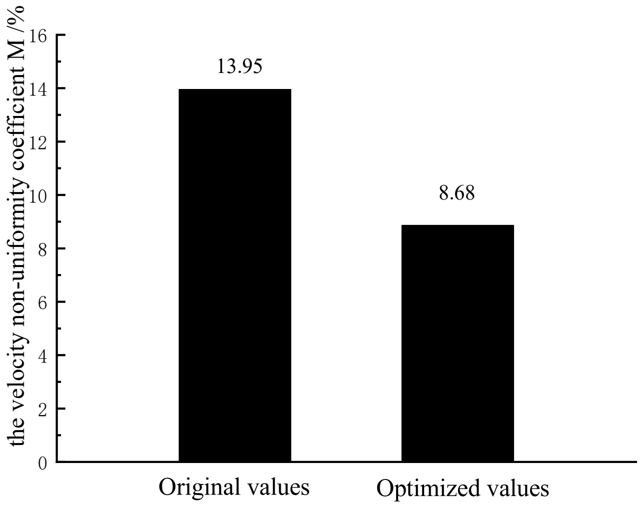

(b) Comparison map of velocity unevenness coefficients

FIGURE 8. Comparison map of original and optimized model results.

It can be seen from Fig. 8(a) and (b) that the interval of the outlet airflow velocity in each column after optimization was 5.30~6.41 m/s. The average flow velocity from the second to fourth column was too high, and although the difference in the outlet flow velocity of each column was reduced compared to the original model, the velocity unevenness coefficient was too high. The outlet flow velocity was initially high and then low, which affected the drying effect. Thus, uniformity in the drying of the dryer could not be achieved. Therefore, it is necessary to further improve the structure of the optimised air distribution chamber to achieve uniformity in the drying of the dryer.

Construction spoiler optimization analysis

According to relevant literature and preliminary basic research, the uniformity of the model flow field can be further improved by constructing a spoiler (Hu et al., 2018). Because the flat spoiler junction has the characteristics of a simple structure, easy installation, and obvious improvement in the outlet velocity distribution (Dai et al., 2013), spoilers of different plate heights, such as one flat spoiler, two flat spoilers, and three flat spoilers were constructed for the optimised model in this study. A flat spoiler was simulated and analysed to determine a reasonable air distribution chamber structure to further improve the drying uniformity of the dryer. According to the numerical calculation, when the spoiler plate height h < 30 mm, the spoiler effect was not significant, and the internal flow field uniformity could not be improved. However, when the spoiler plate height h > 60 mm, the internal flow field uniformity was disturbed, exhibiting a poor effect. Therefore, the spoiler plate height h was selected as 30, 40, 50, and 60 mm, and the spoiler effects were compared by numerical calculation to determine a reasonable air distribution chamber structure. In the numerical calculations, the gas control equations and boundary conditions were consistent with those of the original model.

Figure 9 shows the construction of the spoiler, the simulated flow field of the model, and the average velocity distribution of each column. The spoiler had a thickness of

2 mm and was located at the midpoint of the cavity, 124 mm away from the front and rear cavity plates. As shown in Fig. 9(a), the spoiler was located in the middle of the air distribution chamber and was too far away from the air inlet end. Under the action of the slope of the air distribution chamber, the spoiler was too low, and the hot airflow entering from the air inlet end was inert owing to gas movement. When passing through the spoiler, most of the hot airflow was blocked, and a high airflow velocity zone was formed at the lower end of the spoiler so that the hot airflow directly hit the front end of the outlet. There was insufficient time for the airflow to be exchanged with the surrounding outlets, resulting in a large airflow velocity at the exit. Furthermore, it can be seen from Fig. 9(b) that the hot gas flow had a tendency of "front high and rear low" under the action of spoilers of different heights. Although the unevenness coefficient was slightly lower than that of the original model, the intensity of the outlet airflow in each column was still obvious. Therefore, the position of the spoiler near the inlet end has a significant influence on the outlet flow velocity distribution in the air distribution chamber. The model effect was better when the spoiler plate height was 50 mm. The interval of the outlet airflow velocity in each column was 5.20~5.62 m/s, and the speed unevenness coefficient was 7.95%.

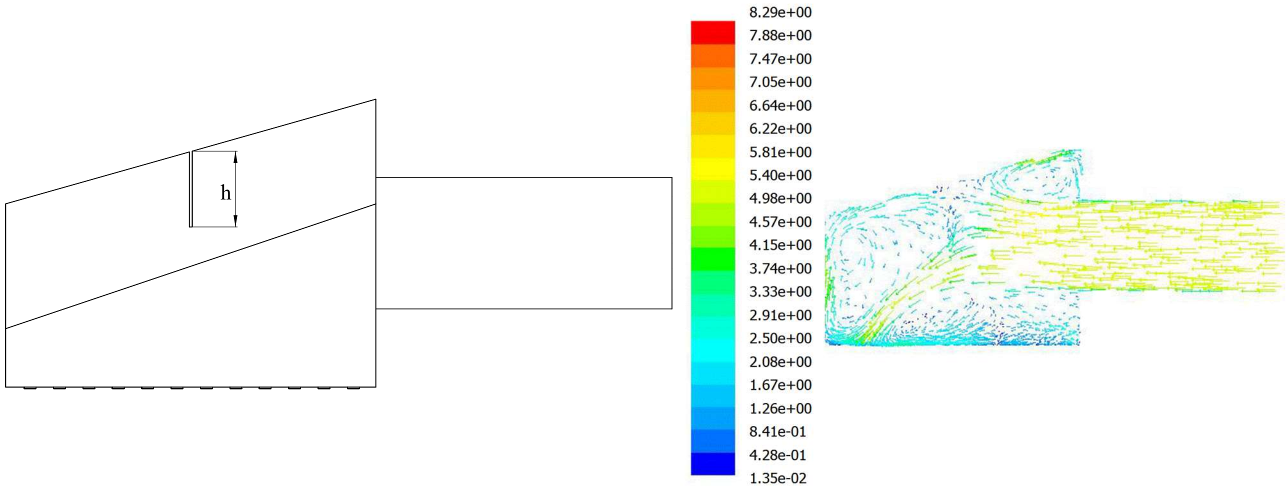

(a) Structure and velocity vector distribution diagrams

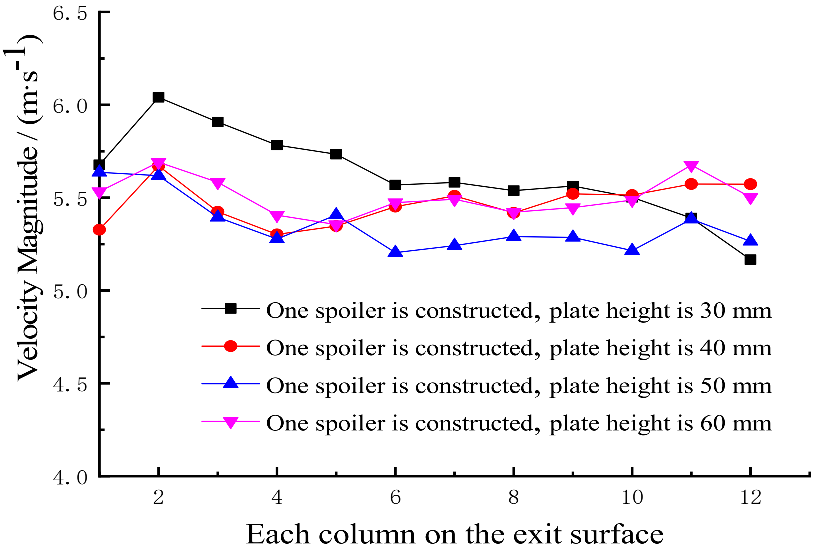

(b) Average velocity distribution of each column exit

FIGURE 9. Model structure and velocity profile of an installed spoiler.

Figure 10 shows the simulated flow field of the model and the average velocity distribution of each column after the construction of two spoilers. The spoilers had a thickness of 2 mm and were located at the 1/3 and 2/3 points between the inlet end and front plate of the cavity, and the plate spacing was 82 mm. As shown in Fig. 10(a), when passing through the two spoilers, the hot airflow entering from the air inlet end formed a low airflow velocity region between the spoilers owing to the inertia of the gas movement, thereby reducing the airflow velocity in the cavity. When the hot airflow was in contact with the front plate of the air distribution chamber, it had sufficient time to blend and fuse to the central region, which reduced the difference between the front and rear outlet flow rates of the air distribution chamber and had a positive impact on the uniformity of the outlet flow rate. As shown in Fig. 10(b), the spoiler plates with different heights had certain differences in the calculation results of the outlet flow velocity of the nozzle group; however, the overall distribution law was approximately evenly distributed. Owing to the influence of the spoiler near the entrance, the exit speeds of the second and third columns were slightly higher than those of the other columns. The model spoiler effect was better when the spoiler plate was 40 mm high. Additionally, the outlet airflow velocity values of each column varied from 5.36 to 5.71 m/s, and the speed unevenness coefficient was 6.05%. The speed difference between the outlets was small, solving the problem of a large speed difference between the nozzles in the original model.

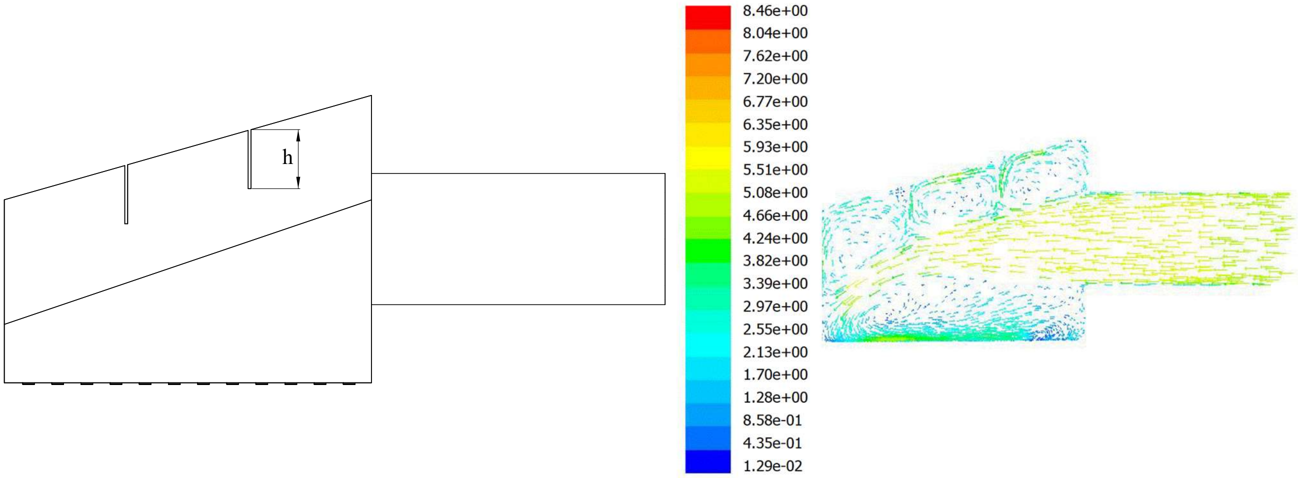

(a) Structure and velocity vector distribution diagrams

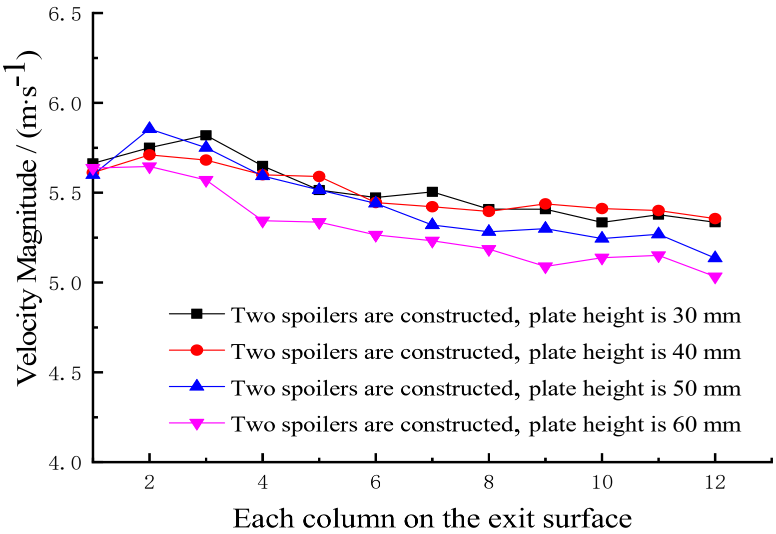

(b) Average velocity distribution of each column exit

FIGURE 10. Model structure and velocity profiles of two installed spoilers.

Figure 11 shows the simulated flow field of the model and average velocity distribution of the outlets of each nozzle row after the construction of three spoilers. The spoilers had a thickness of 2 mm and were located at the 1/4, 1/2, and 3/4 points between the inlet end and front plate of the chamber, with a plate spacing of 61 mm. As shown in Fig. 11(a), the rightmost flat plate was too close to the air inlet end, the spoilers were too high under the action of the inclined surface of the air distribution chamber, and the effective cross-sectional area of the hot air flow was reduced; thus, turbulent flow effect was not obvious after the hot air flow entered from the air inlet end, and the internal flow field uniformity was not significantly improved. Furthermore, as shown in Fig. 11(b), the calculation results of the different plate heights of the three spoilers were different. Among them, plate heights of 30, 40, and 50 mm showed that the average flow velocity of the second column to the fourth column was too high. A speed peak was formed at the front end of the outlet of the air distribution chamber. The middle and back ends tended to be stable, and the trend was essentially the same. When the plate height was 60 mm, the average flow velocity at the front end of the exit was too low, primarily because the right side was too close to the air inlet end. The spoiler was too long and the effective cross-sectional area of the hot gas stream was too large, resulting in an excessively low average flow velocity at the front end of the outlet. In the construction of the three spoilers, the model effect was better when the spoiler plate height was 50 mm. The airflow velocity values of the nozzles varied from 5.13 to 5.61 m/s, and the speed unevenness coefficient was 8.42%. However, the speed difference between the exits of each column was considerably large such that it must be excluded.

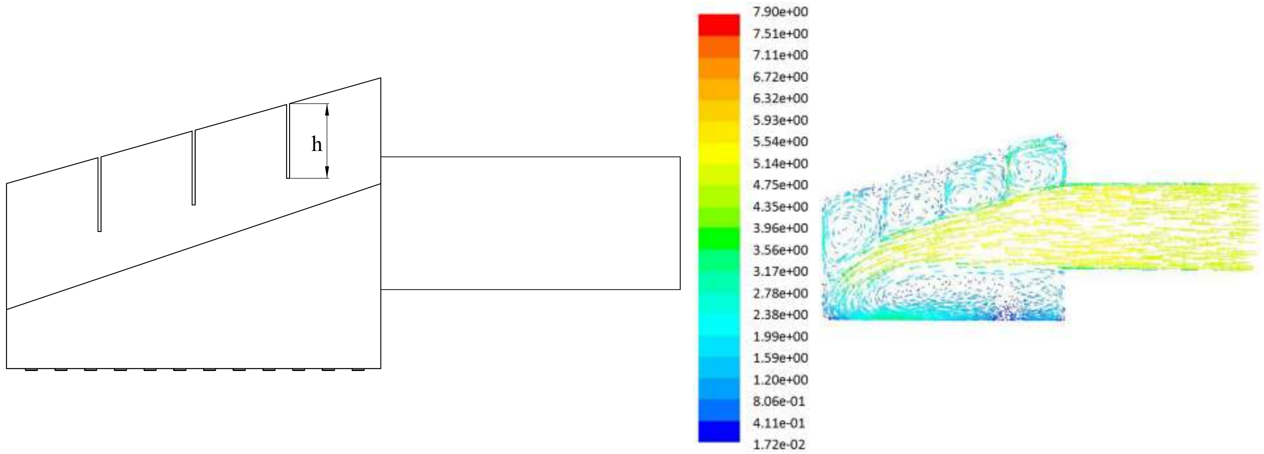

(a) Structure and velocity vector distribution diagrams

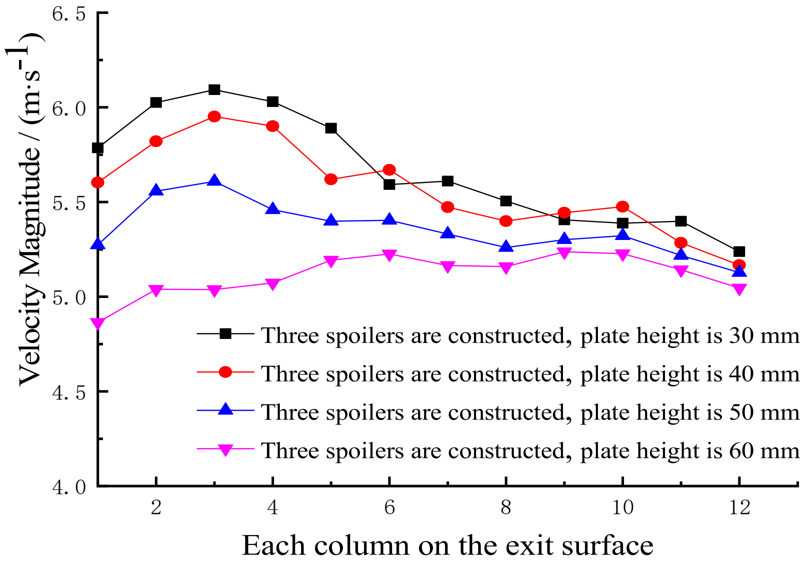

(b) Average velocity distribution of each column exit

FIGURE 11. Model structure and velocity profiles of three installed spoilers

Test verification

Based on the above analysis, after the spoiler was constructed, the flow velocity uniformity of the air distribution chamber was improved. Particularly, when two spoilers were constructed and the plate height was 40 mm, the outlet flow velocity uniformity was optimal. The outlet airflow velocity values of each column varied from 5.36 to 5.71 m/s, and the speed unevenness coefficient was 6.05%. To further demonstrate the accuracy of the numerical calculation, the uniformity of the air distribution chamber of the nutritious bowl-tray microwave–hot-air coupling dryer was verified. Fig. 12 shows the physical object. The inlet velocity of the gas distribution chamber was adjusted to compare the low, medium, and high flow rates. In the microwave–hot-air coupling drying test, an inlet design flow rate of 5 m/s was considered as a high flow rate. The specific values of the low, medium, and high flow rates were 1, 3, and 5 m/s, respectively. The air distribution chamber was consistent with the improved structural spoiler model.

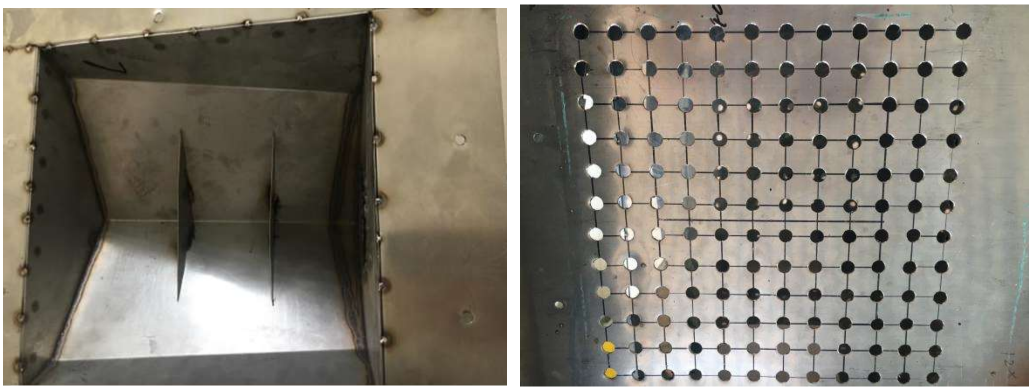

(a) Air distribution room (b) Air distribution room air outlet

FIGURE 12. Physical map of the improved air distribution room.

The hot-air-assisted microwave intermittent drying equipment for the nutritious bowl tray used in this experiment was modified from the YHMW900-100 microwave hot-air coupling multifunctional dryer. Other instruments and equipment included a Junstar 509A stopwatch (Shenzhen Junstar Industrial Co., Ltd.) and MT826 digital anemometer (Hong Kong Metal Electronic Technology Co., Ltd.). After the test results were compared and analysed, the calculated and measured values were compared, as shown in Fig. 13. As shown in the figure, the improved air distribution chamber was essentially the same as the measured value when the inlet speed was 5 m/s. Moreover, the overall distribution was relatively uniform, and the maximum deviation was less than 4% because the value simulation was performed only for the air distribution chamber. The dryer was affected by processing technology, friction loss, and test accuracy error, resulting in numerical deviations. When the inlet velocities were 1 and 3 m/s, the numerical simulation results and experimental data were very close. The overall distribution was essentially the same, and the maximum deviation was less than 2%. It can be clearly seen that the lower the inlet flow rate of the air distribution chamber, the more uniform the outlet flow rate of each column.

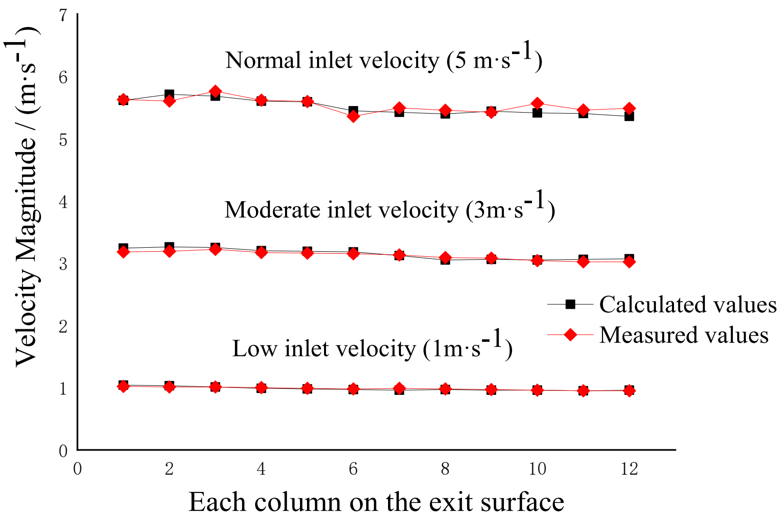

FIGURE 13. Improved model uniformity verification curve.

CONCLUSIONS

1. The air distribution chamber was considered as the object of this study, and ANSYS FLUENT was used to establish the air distribution chamber simulation model. The results showed that the slope angle of the original model of the air distribution chamber was too oblique. After the hot airflow entered from the air inlet end, there was insufficient space in the distribution chamber to distribute the airflow, forming a speed distribution effect of "front high and rear low". The airflow velocity distribution varied from 5.4 to 6.87 m/s, and the original model velocity unevenness coefficient was 13.95%.

2. Through a simulation test, the factors affecting the unevenness coefficient were determined from large to small as follows: $X_3 > X_2 > X_1$. The optimal structure size of the air distribution chamber were as follows: $X_1 =$ 33 mm, $X_2 =$ 108°, and $X_3 =$ 78°. The outlet airflow velocity distribution varied from 5.30 to 6.61 m/s, and the flow velocity of each column was quite different. Hence, the outlet velocity of the air distribution chamber did not satisfy the drying uniformity requirements.

3. In the air distribution chamber with an optimised structure, the construction of two spoilers with a height of 40 mm significantly improved the internal flow field uniformity, and the speed unevenness coefficient was

6.05%, which satisfied the drying uniformity requirements of the dryer. The measured test showed that when the inlet velocity was 5 m/s, the error between the numerical simulation and actual values did not exceed 4%, and the lower the inlet flow velocity of the air distribution chamber, the more uniform the outlet flow velocity of each column. The above results can provide theoretical support for the design and industrial production of microwave–hot-air coupling dryers and technical support for the industrial production of nutritious bowl trays.

ACKNOWLEDGEMENTS

This research was funded by the China Postdoctoral Science Foundation (2016M601404), Heilongjiang Provincial Natural Science Foundation of China (C2015037), National Key Research and Development Program (2016YFD800602), National Science and Technology Support Program Task Book (2014BAD06B01), Heilongjiang Land Reclamation Bureau Science and Technology Project (HNK135-03-02-03), and Zhaoqing University Scientific Research Fund Funding Project (202015).

REFERENCES

Cai JP, Xiao LP, Liu MH, Ye Y, Li T, Chen X (2018) Development Status and Prospect of Rice Mechanization Transplanting Technology. Journal of Agricultural Mechanization Research 40(10): 6-10+81.

Chen HG, Dong, XW, Zhang JJ (2005) Development of rice seedling tray in pot. Modernizing Agriculture (09): 31-32.

Chen XK, Yang KJ (2017) Effects of Different Seedling Trays on Quality and Yield of Rice Seedlings. Modernizing Agriculture (04): 35-36.

Dai JW, Xiao HW, Bai JW, Zhang Q, Xie L, Gao Z (2013) Numerical simulation and optimum design on airflow distribution chamber of air-impingement jet dryer. Transactions of the Chinese Society of Agricultural Engineering 29(03): 69-76+295.

Ding TH, Cao SM, Xue XY, Ding S, Zhou L, Qiao B (2016) Simulation and experiment on single-channel and double-channel airflow field of orchard sprayer. Transactions of the Chinese Society of Agricultural Engineering 32(14): 62-68+315.

Guo DS, Huang CH (2016). Spatial and Temporal Distribution of Crop Straw Resources in Past 10 Years in China and Its Use Pattern. Southwest China Journal of Agricultural Sciences 29(04): 948-954.

Han WT, Wu PT, Yang Q, Feng H (2005) Advances and comparisons of unifor mity evaluation index of sprinkle irrigation. Transactions of the CSAE (09): 172-177.

Han YJ, Chen HT, Liu LX, Li H (2011) Optimization of technical parameters for preparing fiber from rice straw. Transactions of the CSAE 27(04): 281-286.

Hassan J, Mohamed T, Mohamed W, Alawee W (2014) Modeling the Uniformity of Manifold with Various Configurations. Journal of Fluids: 1-8.

Horuz E, Bozkurt H, Haluk K, Medeni M (2017) Simultaneous application of microwave energy and hot air to whole drying process of apple slices: drying kinetics, modeling, temperature profile and energy aspect. Heat and Mass Transfer 54(2): 425-436.

Hu X, Feng J, Zhao LX, Guo Z, Yao Z, Luo J (2018a) Research Progress of Dry Anaerobic Fermentation Reactors and Its Process Control Technique. China Biogas 36(02): 68-75.

Hu SC, Xiong HL, Zeng Q (2018b) Optimization of velocity uniformity of duct in veneer drying room. Manufacturing Automation 40(03): 125-128+133.

Jiang EC, Sun ZF, Pan ZY, Wang L (2015) Performance Analysis and Operational Parameters Optimization of Deposition Chamber to Clean Super Rice in Stripper Combine Harvester. Transactions of the Chinese Society for Agricultural Machinery 46(01): 100-105.

Kalman EL, Lofvendahl A, Winquist F (2000) Classification of complex gas mixtures from automotive leather using an electronic nose. Analytica Chimica Acta 403(1): 31-38.

Knopp T, Alrutz T, Schwamborn D (2006) A grid and flow adaptive wall-function method for RANS turbulence modelling. Comput Phys 220(1): 19-40.

Lei XL, Li HX, Zhang Q, Wang T (2011) Regulation performance and optimal design of the gas adjust-screen in boiler steering rooms. Journal of Huazhong University of Science and Technology 39(10): 128-132.

Li LH, Zhang W, Wang C, Zhang J (2014) High strength structural design and influence test for rice seedling-growing bowl tray made of paddy-straw. Transactions of the Chinese Society for Agricultural Machinery 45(11): 88-97.

Li YJ, Wang FJ (2007) Assessment of two-equation turbulence modeling for hydrofoil flows at high reynolds number. Transactions of the Chinese Society for Agricultural Machinery (12): 45-48+52.

Li YY, Hu CR (2008) Experiment design and data processing. Beijing, Chemical Industry Press, p134-136.

Liu HJ, Liu JF, Hao JJ, Li J (2012) Biomass seeding bowl and molding equipment. Transactions of the Chinese Society for Agricultural Machinery 43(02): 52-54+74.

Ma X, Ma CL, Zhang SQ, Sun Y, Sun T (1997) The study on transplanting unit of the mechanical type air-pruning tray seedling growing. Transactions of the CSAE S1: 272-275.

Pan M, Zeng D, Tang Y, Chen D (2009) CFD-based study of velocity distribution among multiple parallel microchannels. Journal of Computers 4(11): 1133-1138.

Qu LX, Wang FJ, Cong GH, Yao Z (2011) Pressure fluctuations of the impeller in a Double-suction centrifugal pump. Transactions of the Chinese Society for Agricultural Machinery 42(09): 79-84+78.

Sun BC, Li MG (2013) ANSYS FLUENT 14.0 Optimal analysis and design. Beijing, Mechanical Industry Press.

Tang M, Zhang S, Wang D, Liu Y, Zhang Y, Wang L, Liu C (2019) CFD simulation of gas flow field distribution and design optimization of the tridimensional rotational flow sieve tray with different structural parameters. Chemical Engineering Science 201: 34-49.

Tian ST, Gao ZJ (2009) Improved design of airflow distribution chamber in air-impingement oven based on fluent. Modern Food Science and Technology 25(06): 612-616.

Wang H, Mu S, Li TC, Wu J, Xie Y, Chen X, Liu S (2018) Study on the combination of hot air microwave and intermittent drying process of chinese wolfberry based on response surface methodology. Modern Food Science and Technology 34(02): 134-140+110.

Wang JW, Tang H, Wang JF (2017) Comprehensive utilization status and development analysis of crop straw resource in Northeast China. Transactions of the Chinese Society for Agricultural Machinery 48(05): 1-21.

Xu P, Shi YZ, Fu ZC (2005) Optimization design of gas distribution chamber in Wall-mounted Gas Boiler. Gas & Heat (06): 5-8.

Yakhot V, Orszag S (1986) Renormalization group analysis of turbulence: basic theory. Journal of Scientific Computing 1(1): 1-11.

Yu HM (2015) Study on drying mathematical model of hawthorn using microwave coupled with hot air and drying machine design, Changchun, Jilin University.

Yu HM, Li HY, Wang C, Li HL, Zhang XY, Liang Q, Yu BB (2020) Simulation analysis of flow field uniformity in air distribution room of rice seedbed microwave hot air coupling dryer. Journal of Agricultural Mechanization Research 42(02):15-21.

Yu HM, Li HY, Zhang FX, Wang HY, Zhang XY, Liu HJ (2021) Optimization of hot air-assisted intermittent microwave drying technology for straw-based nutrient seedling-growing bowl tray. International Agricultural Engineering Journal 30(02): 47-66.

Yu HM, Wang C, Han ZX, Sun Y, Zhang W, Hu J, Liu T (2013) Optimization of steam drying conditions for seedling-growing tray made of paddy-straw. Transactions of the Chinese Society of Agricultural Engineering 29(21): 40-49.

Yu HM, Wang C, Xie QJ, Sun Y, Zhang W, Hu J, Che G (2014) Development and performance experiment of steam drying device of seedling-growing tray made of paddy-straw. Transactions of the Chinese Society of Agricultural Engineering 30(01): 25-33.

Yu HM, Zuo CC, Xie QJ (2015a) Parameter optimization for microwave coupled with hot air drying process of hawthorn slices using response-surface methodology. International Journal of Agricultural & Biological Engineering, 8(2): 121-134.

Yu HM, Zuo CC, Xie QJ (2015b) Drying characteristics and model of chinese hawthorn using microwave coupled with hot air. Mathematical Problems in Engineering 2015: 1-15.

Yu Y, Zhang JM, Jiang LT (2008) FLUENT introduction and advanced courses. Beijing, Beijing Institute of Technology Press.

Zhang XY, Wang C, Li LH, Zhang W (2013) Preparation technology and parameters optimization for seedling-growing bowl tray made of paddy straw. Transactions of the Chinese Society of Agricultural Engineering 29(05): 153-162.

Zheng C, Liu Y, Wang H, Zhu H, Liu Z, Ji R (2015) Structural optimization of downhole fracturing tool using turbulent flow CFD simulation. Journal of Petroleum Science and Engineering 133: 218-225.

Zhou LF, Zhang XX, Lv XL, Ding S (2012) Numerical simulation and experiment on wind performance of disc atomizer. Transactions of the Chinese Society for Agricultural Machinery 43(10): 72-75+81.

Zhou YN, Zhou JL, Huang FY, Zhou L, Wang XY, Li CY (2021) Simulation and analyze of mobile bee-keeper flow field based on CFD. Building Energy & Environment 40(11): 80-84.